

Annual Review of Physical Chemistry
**Interferometric Scattering
Microscopy**

Gavin Young and Philipp Kukura

Physical and Theoretical Chemistry Laboratory, Department of Chemistry, University of Oxford, Oxford OX1 3QZ, United Kingdom; email: gavin.young@chem.ox.ac.uk, philipp.kukura@chem.ox.ac.uk

Annu. Rev. Phys. Chem. 2019. 70:301–22

First published as a Review in Advance on
April 12, 2019

The *Annual Review of Physical Chemistry* is online at
physchem.annualreviews.org

<https://doi.org/10.1146/annurev-physchem-050317-021247>

Copyright © 2019 by Annual Reviews.
All rights reserved

**ANNUAL
REVIEWS CONNECT**

www.annualreviews.org

- Download figures
- Navigate cited references
- Keyword search
- Explore related articles
- Share via email or social media

Keywords

interference, single molecule, label-free, self-assembly, single-particle tracking, mass measurement

Abstract

Interferometric scattering microscopy (iSCAT) is an extremely sensitive imaging method based on the efficient detection of light scattered by nanoscopic objects. The ability to, at least in principle, maintain high imaging contrast independent of the exposure time or the scattering cross section of the object allows for unique applications in single-particle tracking, label-free imaging of nanoscopic (dis)assembly, and quantitative single-molecule characterization. We illustrate these capabilities in areas as diverse as mechanistic studies of motor protein function, viral capsid assembly, and single-molecule mass measurement in solution. We anticipate that iSCAT will become a widely used approach to unravel previously hidden details of biomolecular dynamics and interactions.

1. INTRODUCTION

Numerical aperture: quantifies the range of angles over which a lens can collect light; dictates how tightly a lens can focus light

Fluorescence: having absorbed light, some substances spontaneously emit light of a different wavelength in a spin-allowed transition

The primary objective of microscopy is to visualize structure and dynamics on small length scales. Our perception of the meaning of the word small in the context of what can be imaged has evolved dramatically since Hooke's observation of individual cells 350 years ago (1), all the way to clear images of individual atoms (2). The use of visible light to image the species of interest has been and continues to be important in the life science context, owing to its comparatively noninvasive nature and three-dimensional imaging capability. Frustratingly, however, light microscopy has until relatively recently been restricted to modest gains in resolution and sensitivity, largely limited by the achievable numerical aperture and the resulting mismatch between the area to which light can be confined and the size of even relatively large molecules (**Figure 1a**).

Being able to visualize the smallest features ultimately comes down to addressing three challenges: resolution, specificity, and sensitivity. Here, we focus on imaging sensitivity, which is determined by a combination of two factors: the ability to detect a weak signal and the ability to distinguish that signal from any background. The most intuitive way to achieve the latter involves removing all other objects, i.e., trapping in a vacuum, which led to the first observation of individual ions (3). It took almost another decade until similar sensitivity levels were reported in the condensed phase, using absorption as a contrast mechanism in combination with a sophisticated double-modulation approach at cryogenic temperatures (4). Soon thereafter, the same molecular system was investigated using fluorescence detection as in the original ion work, demonstrating significantly enhanced signal-to-noise ratios (SNRs) compared with the absorption case but with a considerably simpler experimental setup (5). The difference in achievable SNRs between the

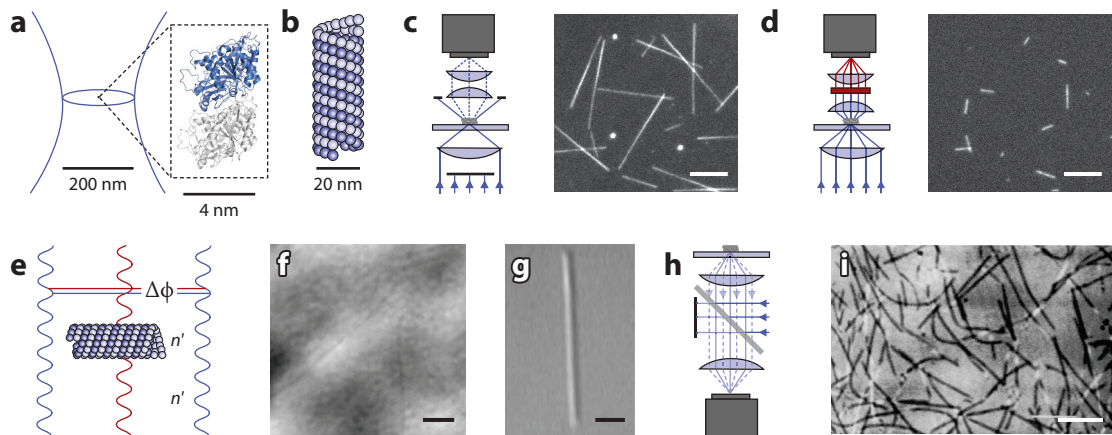


Figure 1

Sensitivity limits of light microscopy illustrated with tubulin and microtubules. (a) Illustration of the size mismatch between the diffraction-limited area of visible light focused with a high numerical aperture objective and that of the tubulin dimer. (b) Simplified microtubule structure. (c) Schematic of a typical dark-field microscope and example image of individual microtubules acquired using such a microscope. Scale bar: 5 μm . (d) Schematic of a fluorescence microscope operating in transmission mode and an example image of fluorescently labeled microtubule seeds. Scale bar: 5 μm . (e) Schematic of interference-based optical detection of a nano-object. (f) Phase contrast image of microtubules. Scale bar: $\sim 5 \mu\text{m}$. (g) Differential interference contrast image of a single microtubule. Scale bar: 2 μm . (h) Schematic of reflection-based interference microscopy. (i) Image of individual microtubules taken on a laser-scanning confocal microscope in reflection mode. Scale bar: 4 μm . Panel *f* adapted from Reference 13 with permission; copyright 2017 American Chemical Society. Panel *g* adapted from Reference 7 with permission. Panel *i* adapted with permission from Reference 23.

two experiments is representative of the ease with which one can remove background signatures arising from the bulk.

1.1. Scattering and Absorption as a Contrast Mechanism

The challenge in moving from fluorescence toward the more universal extinction as a contrast mechanism rests on our ability to reject background signatures that overpower the signal of interest. In fluorescence detection, the ability to suppress illumination light by more than six orders of magnitude using optical filters while detecting at a different wavelength with essentially no losses generates a vacuum-equivalent scenario. The object becomes completely isolated from other optical signals, as long as none of the surrounding molecules and optics fluoresce at the detection wavelength. It is therefore not surprising that fluorescence detection has been the dominant mechanism for single-molecule optics since its inception and has become a routine approach through the directed improvement of associated detectors and optics.

Efficiently separating illumination and detection, however, does not necessarily require a difference in wavelength between the two processes. Using the simple concept of orthogonal illumination and detection pathways, Siedentopf & Zsigmondy (6) recorded optical signatures from nanometer-sized gold colloids as early as 1902 using what they called an ultramicroscope. The general concept of removing excitation light while detecting scattered light has become known as dark-field microscopy, which has traditionally been the gold standard for ultrasensitive light microscopy beyond fluorescence. As an example, dark-field observation of individual microtubules (**Figure 1b,c**) can produce images of near-identical quality to those achievable with fluorescence staining (**Figure 1d**) (7). Given the similarity of these images in terms of their contrast, the immediate question arises as to why dark-field microscopy cannot detect single molecules if fluorescence can. Although factors such as labeling density affect the fluorescence contrast to some degree, a key difference is how the signal magnitude scales with the number of molecules present.

Assuming for simplicity that every tubulin dimer is fluorescently labeled and given that the structure of microtubules implies the presence of approximately 300 dimers per diffraction-limited spot (**Figure 1b**), we would accordingly expect the signal to drop 300-fold in fluorescence detection when comparing the signals from a microtubule and a single tubulin dimer. By contrast, the dark-field scattering signal scales with the square of the object volume, which in this case is roughly equivalent to the square of the number of proteins, amounting to a signal drop of $\sim 10^5$. Ultimately, this dramatic signal scaling with object size makes the detection of single molecules in pure scattering so challenging. The problem is not that extinction signals become intrinsically too small to detect, as we know from the observation of single atoms in vacuum (8), but rather that it becomes increasingly difficult to detect these signals in the presence of background light caused by the sample or imperfections in the optics. Even if the background were constant and could be subtracted, the measurement would have to be performed with extremely high dynamic range to visualize and quantify the tiny single-molecule signal over the dominant background.

1.2. Interference-Based Microscopy

The drastic drop in scattering signal with particle volume can be partially addressed by employing an interferometric detection scheme, because the interferometric signal scales linearly with object size compared with a square dependence for pure scattering (9). Here, the object is detected as a consequence of interference between background light and light phase-shifted by interaction with the object (**Figure 1e**). That such an approach may indeed be worth pursuing in the context of visualizing small objects was already confirmed by the first report on single-molecule detection

Extinction: the combined effect on radiation of absorption and scattering by a substance

Shot noise:

Poisson-distributed noise associated with counting independent and random discrete events, such as photons arriving at a detector

(4), which was enabled by modulating the interference between light interacting with the molecule and background light. Taken together, interference thus seems well suited for ultrasensitive optical microscopy down to the single-molecule level, with the continuing caveat of sufficient background suppression.

Perhaps the first microscope to explicitly make use of interference as a contrast mechanism was the phase contrast microscope conceived in 1935 by Zernike (10), which introduces a phase shift to the transmitted light in a conventional microscope to increase the contrast of transparent objects. This was followed in the 1950s by differential interference contrast microscopy (11, 12), where the interference takes place between a pair of slightly displaced beams to reveal interfaces between regions of different refractive index. A major advantage of both approaches is the use of common path interferometry, where the two interfering light fields travel along almost identical routes, minimizing the influence of external perturbations. Nevertheless, images of microtubules using these contrast mechanisms fail to achieve image quality comparable with that of dark-field microscopy: In phase contrast, microtubules are barely visible owing to illumination, transmission, and detection inhomogeneities (**Figure 1f**) (13), whereas differential interference contrast improves the image quality (**Figure 1g**) (7) but still with inferior SNR compared with dark-field imaging. Although such transmission-based schemes have struggled to reach the extreme sensitivity levels required for single-molecule detection, there have been significant developments using advanced illumination and detection schemes, which are particularly powerful for label-free imaging of cellular structures (14, 15).

Operating interference-based microscopy in reflection rather than transmission is advantageous for the detection of small objects, because the majority of incident light passes the sample unaffected, while only a small portion is reflected (**Figure 1b**). Assuming that light scattering from subdiffraction objects is the same in the forward and backward directions, the combination of weakly reflecting illumination and backscattered light results in enhanced interferometric contrast. It is important to realize that this approach does not improve the SNR of the measurement. The contrast simply increases at the expense of the total number of detected photons, resulting in the same SNR for shot noise-limited detection (16).

There have been numerous implementations of common path interferometry in reflection for microscopic contrast, taking advantage of different illumination and detection schemes, all sharing the same underlying idea. A transparent substrate supporting the sample is illuminated through the same objective lens as is used for imaging. A small portion of the incident light is reflected at the interface between the glass and the sample, serving as a reference field. The majority of the incident light propagates past the interface and interacts with objects in the sample. The back-reflected light from the interface and some of the light scattered by the sample are collected by the objective lens and used to form an image (**Figure 1b**). The detected intensity, I_{det} , at a given point in the image is then given by

$$I_{\text{det}} = I_{\text{inc}}[r^2 + |s|^2 + 2r|s| \cos(\varphi)], \quad 1.$$

where I_{inc} is the incident intensity, r^2 is the reflectivity of the glass-water interface, s is the scattering amplitude of the object, and φ is the phase difference between the reflected and scattered fields. For Mie scattering by a spherical particle, the scattering amplitude can be written as

$$s = \eta \varepsilon_m \pi \frac{D^3}{2} \frac{\varepsilon_p - \varepsilon_m}{\varepsilon_p + 2\varepsilon_m}, \quad 2.$$

where $\varepsilon_{m/p}$ are the dielectric functions of the surrounding medium/particle, respectively; D is the diameter of the spherical particle; and η is a constant factor accounting for the detection

efficiency of the setup. Here, the origin of the intensity scaling for pure versus interferometric detection discussed above becomes immediately clear: Whereas the pure scattering term, $|s|^2$, scales with the square of the volume of the scattering object, the interferometric term scales linearly, causing a much slower signal drop with decreasing object size. It is this interferometric contribution that is of particular interest for ultrasensitive imaging.

Initially, it was the phase change caused by an optical path difference between the two fields that attracted most interest and was used to measure cellular adhesion in a method termed interference reflection microscopy (17). Developments in the experimental implementation, primarily the introduction of the antiflex method to reduce stray reflections from optical components (18), and in the theoretical framework of the technique (19) followed, though the inherent optical complexity of the biological cell limited interpretation of the images obtained to a mostly qualitative nature (20). Subsequent work was thus aimed at better-defined model systems, enabling quantitative measurements on colloidal particles, giant unilamellar vesicles, and lipid bilayers (21, 22), with the technique by then known as reflection interference contrast microscopy.

Speckle: apparently random intensity pattern produced by the interference of a set of wavefronts, such as those produced by scattering from a rough surface

1.3. Ultrasensitive Extinction Microscopy

Although the improved scaling of the interferometric scattering signal versus that of pure scattering assists in the detection of weakly scattering objects, the associated signals still drop linearly with volume, making very small objects such as single molecules difficult to detect. Under ideal experimental conditions, the only noise source would be the shot noise associated with counting photons. Were one to realize such ideal detection, the use of lasers as an illumination source could be advantageous owing to the high incident power densities of monochromatic light that they enable, despite bringing additional difficulties associated with coherent illumination, such as a risk of increased speckle corrupting the image.

The first explicit example of imaging subdiffraction objects in a reflected light microscope using laser illumination made use of a laser-scanning confocal microscope that was equipped with a beam splitter, rather than the more conventional dichroic mirror in fluorescence imaging, to study microtubule dynamics (**Figure 1i**) (23). Although performing a quantitative comparison is difficult, it appears that the interferometric contrast is enhanced compared with differential interference contrast (**Figure 1g**) and the SNR is at least qualitatively comparable with dark-field imaging (**Figure 1c,i**). Given these results, single-molecule detection sensitivity does not seem completely impossible. Nevertheless, interest in this approach to interferometric detection essentially vanished with the influx of genetically encodable fluorescent proteins (24) and the immense promise of fluorescent imaging for cellular and single-molecule imaging. Interest in fluorescence-free imaging of nanoparticles only reemerged alongside the advent of nanoscience and when the fundamental limitations associated with fluorescence-based methodologies were encountered.

A step change in detection sensitivity was achieved by an absorption-mediated modulation approach called photothermal microscopy, enabling the observation of 5-nm gold particles (25). Here, background suppression was achieved by a contrast mechanism based on a phase shift induced by local heating of the sample and ensuring that this heating was exclusively due to light absorption by the nanoparticle of interest. Subsequently, Lindfors et al. (26) demonstrated detection and spectroscopic investigation of gold nanoparticles (GNPs) as small as 5 nm in diameter for interferometric imaging in reflection with a supercontinuum laser source. Reverting to the illumination scheme used in Reference 23 allowed for more rapid monochromatic imaging, high-speed detection and visualization of nonmetallic objects such as microtubules (27) and viruses (28), and implementation of wide-field imaging (27).

Point spread function

(PSF): response of a microscope to a point source, approximately an Airy disk limited in width to ~ 200 nm for visible light and a high numerical aperture objective

Localization

precision: precision with which the center of mass of an object can be determined

Photoblinking:

switching between bright and dark states of a fluorophore, typically as a result of the photophysics of the emitter

Photobleaching:

permanent cessation of a fluorophore's emission as a result of photochemical alteration of the emitter

1.4. Interferometric Scattering Microscopy

The term interferometric scattering microscopy (iSCAT) was coined in the context of a study reporting on the diffusional dynamics of individual viruses on supported lipid bilayers (29). Although technologically similar to Reference 23 in recording the interference of scattered and back-reflected laser light from a sample with an inverted microscope, it introduced a few concepts that have since been crucial to the evolution of the technology. Principal among these is the, in hindsight, trivial realization that for shot noise-limited detection the SNR of an interferometric signal, S , scales as $S \propto N^{1/2}$, where N is the total number of detected photons. Given that N for a given exposure time is directly proportional to the illumination intensity, the SNR could therefore in principle be improved indefinitely by simply detecting more photons, by increasing either the laser power or the exposure time. The underlying challenge, therefore, is to maintain shot noise-limited imaging performance. This was addressed in two ways, which have and continue to remain central to all iSCAT experiments: (a) wide-field detection combined with speckle-free illumination to eliminate image noise caused by laser-based fluctuations that otherwise make shot noise-limited detection impossible and (b) efficient (digital) background subtraction, in particular of residual substrate signatures, spurious reflections, and illumination inhomogeneities.

The result of this evolution is a light microscope capable of—at least in principle—detecting and localizing any changes in local optical properties relative to the surrounding medium (see Equation 2). We illustrate the resulting unique capabilities of iSCAT in three application areas: (a) high-speed and/or highly accurate single-particle tracking (SPT) of GNPs or similarly strong scatterers (Section 2); (b) imaging biological nano-objects made of lipids or peptides and their (dis)assembly dynamics (Section 3); and (c) detection, imaging, and mass measurement of single unlabeled proteins (Section 4).

2. SINGLE-PARTICLE TRACKING

SPT interrogates the motion of single molecules or larger assemblies at a level of detail inaccessible to ensemble techniques (30). In its fluorescence-based implementation, the object of interest is typically labeled with a dye molecule, fluorescent protein, or semiconductor quantum dot. The optical image of a subdiffraction species returns the point spread function (PSF) of the microscope centered on the location of the object. Although the full width at half maximum of the PSF is typically on the order of 200 nm for visible light and a high numerical aperture objective lens, finding the center of mass of the PSF, for example, by fitting a two-dimensional Gaussian function, returns the position of the emitter with a precision much higher than the resolution of the microscope. The achievable precision in the absence of noise sources other than shot noise can be approximated as $\sigma/N^{1/2}$, where σ is the standard deviation of the Gaussian and N the number of detected photons (31). In this way, localization precision on the order of a few nanometers is achievable for $N > 10^4$ (32).

The key advantage of fluorescence-based SPT is its compatibility with live-cell imaging because of its powerful background rejection capability and the possibility of using molecular-sized dye labels or genetically encodable fluorescent proteins (24). Photoblinking and photobleaching, however, limit the total observation time and can produce gaps in the acquired trajectories, resulting in poor statistics. More fundamentally, however, optical saturation caps the maximum achievable photon flux from single emitters. Combined with the dependence of localization precision on photon count mentioned above, this results in a rule of thumb that the achievable spatiotemporal precision is on the order of $1 \text{ nm/Hz}^{1/2}$. Although these limitations can be addressed by reducing the observation duration per trajectory (33, 34) or using advanced illumination approaches (35), the majority of single-emitter-based studies exhibit comparable performance characteristics (32, 36–40).

These limitations are absent for iSCAT, as for all scattering-based approaches, because scattering labels do not bleach or blink, nor do they saturate regardless of illumination power. If the $\text{SNR} \propto S \times N^{1/2}$, as enabled by background subtraction and shot noise-limited detection, then one can maintain a given localization precision irrespective of exposure time, which determines the time resolution, by proportionally increasing the incident light intensity. As a result, within the limits set by photodamage, one can achieve essentially arbitrary combinations of localization precision and temporal resolution for high-speed (Section 2.1) and high-precision (Section 2.2) SPT. This comes at the cost of a requirement for larger labels, usually on the order of 20-nm-diameter GNPs for in vitro and 40-nm diameter or larger for cellular studies (Section 2.3). At the same time, however, label-free imaging of biological nanoparticles can be performed directly, obviating the need for labeling altogether (Section 2.4).

2.1. High-Speed Single-Particle Tracking

The capabilities of iSCAT for SPT are well introduced by recent experiments on the processivity of myosin 5, a molecular motor that has been studied in much detail at the single-molecule level over the past decades (41). Using single-molecule fluorescence, it has been shown to walk in a hand-over-hand fashion along actin, taking ~ 74 -nm steps (Figure 2*a*) and consuming one ATP

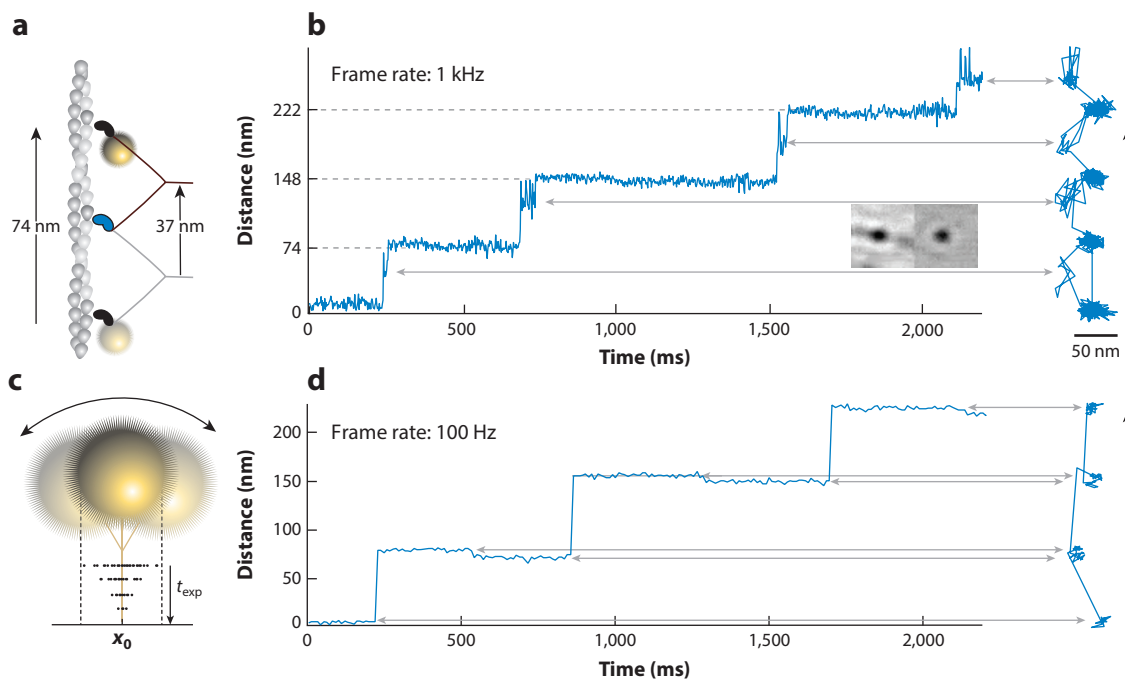


Figure 2

Tracking of molecular motors with gold nanoparticle labeling with high spatial precision and temporal resolution. (a) Schematic of a gold-labeled myosin 5 motor stepping along an actin filament. (b) Distance-time trace and accompanying XY trajectory of a myosin 5 molecule stepping along actin, imaged at 1 kHz. The transient state when the motor takes a step is localized to one side of the actin filament. (Inset) Image of a 20-nm gold nanoparticle label before and after background subtraction. (c) Schematic of the concept of temporal averaging to improve localization precision, through averaging the motion of the scattering label. (d) Distance-time trace and accompanying XY trajectory of a myosin 5 molecule stepping along actin, after frame averaging to 100 Hz. A small transition can be observed while the labeled head is bound to actin. Panels *a*, *b*, and *d* adapted from Reference 45.

molecule per step (32, 42, 43). As a consequence of the limitations in spatial precision and temporal resolution achievable with fluorescence imaging, these experiments could provide information on the motor only while bound to the underlying actin filament, leaving much of the stepping mechanism in the dark. Using iSCAT imaging of 20-nm gold labels attached to one of the motor domains revealed detailed signatures of a previously reported intermediate state (44) persistently to one side of the actin filament (**Figure 2b**). This transient state exhibited kinetics associated with ATP hydrolysis, which is required before the moving head can rebind to actin to complete the step, suggesting that it is a signature of the step being taken. In combination with a series of control experiments, this finding led to a model for the efficiency of myosin 5 processivity, based on restricted relative motion between the two heads of the protein (45). The clear observation and characterization of this state was enabled by the simultaneous nanometer spatial precision and millisecond temporal resolution, which are highly beneficial for mechanistic studies of motor proteins (46, 47).

Although these imaging speeds are sufficient to reveal many new details of motor protein motility, where the relevant timescales are determined by the mechanochemical cycle of the protein, following processes such as diffusion in lipid bilayers requires much higher temporal resolution (48). The absence of saturation in the scattering signal also allows access to these temporal regimes with iSCAT, enabling not only detection (27) but also nanometer-precise tracking with submillisecond exposure times (16, 49, 50). Frame rates have even approached 1 MHz with an appropriately fast camera (51). Accessing these temporal and spatial domains with SPT is particularly important, because it allows for the observation of transient events (52, 56).

2.2. High-Precision Single-Particle Tracking

Aiming for ever-higher temporal resolution with label sizes on the order of several tens of nanometers, however, contains a potential pitfall: One begins to observe not only the motion of the object to which the label is attached but also the motion of the label itself (50). As a result, even if the nominal localization precision is high at very low exposure times, trajectories become affected by the motion of the particle about its attachment point, which is superimposed onto the motion of the object of interest. Moving in the opposite direction of longer integration times, for example by temporal averaging of frames, effectively eliminates this effect because the label motion averages out and enables very high SNRs through large total numbers of detected photons per exposure and thus very high localization precision (**Figure 2c**). One therefore has either to accept slightly lower than theoretically achievable localization precision (45) or to sacrifice some temporal resolution for spatial precision (53).

As an example, in the case of myosin 5, reducing the imaging speed from 1 kHz to 100 Hz improved the localization precision to 1.6 nm. As a result, the traditional distance versus time traces now exhibited not only the expected 74-nm step of the labeled head but also an additional, much smaller backward movement of the label coinciding with stepping of the unlabeled head (**Figure 2d**). The key outcome here is the ability to maintain few-nanometer localization precision even at speeds almost 100-fold higher than achievable with single-molecule fluorescence for prolonged imaging, thereby accumulating sufficient statistics to clearly visualize previously hidden transitions. An additional salient point is that the concept of repeated measurements can be reused to improve precision with respect to the localization of the bound states, with subnanometer precision possible in principle.

2.3. Tracking Molecules on Cells

High-performance SPT, in addition to detecting sufficient photons, rests on the ability to estimate and remove the background, not just from the optical setup but also from scattering within

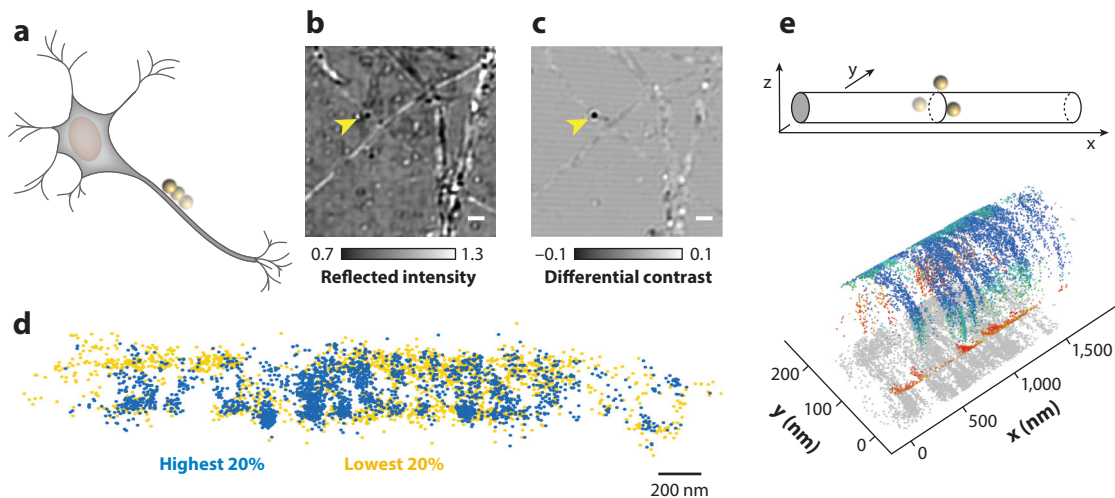


Figure 3

Interferometric scattering microscopy (iSCAT) tracking on cells. (a) Schematic of gold nanoparticle (GNP) tracking on an axon of a neuronal cell. (b) Raw iSCAT image of a 40-nm GNP-labeled membrane protein on a neuronal cell. The yellow arrow marks a GNP. Scale bar: 2 μm . (c) Background-subtracted image of a 40-nm GNP-labeled membrane protein on a neuronal cell; a yellow arrow marks the GNP. Scale bar: 2 μm . (d) Selected localizations from 2-kHz trajectory of 40-nm GNP-labeled glycosylphosphatidylinositol-green fluorescent protein on an axon. The 20% of all localizations exhibiting the highest confinement are shown in blue, whereas the 20% exhibiting the lowest confinement are shown in yellow. (e) Schematic of a three-dimensional reconstruction from the geometry of the neurite and example three-dimensional trajectory. Panels b–e adapted from Reference 54 with permission from Elsevier.

the sample. The examples considered so far are reconstituted systems where the sample-specific background can be well controlled. More highly scattering environments such as living cells, however, prove to be more of a challenge, although such measurements are possible provided that the background is small and varies much more slowly than the motion of the particle of interest. As an example, it has proven possible to track 40-nm GNP-labeled membrane proteins with 3-nm localization precision at 40 kHz on thin regions of U2OS cells and the axons of neuronal cells (**Figure 3a–c**) (54). In agreement with the arguments outlined above concerning the balance between temporal resolution and achievable localization precision as a consequence of label motion, temporal averaging to 2-kHz frame rate revealed signatures of compartmentalized diffusion. The resulting periodicity on the order of 200 nm (**Figure 3d**) matched the periodicity of actin-spectrin rings previously reported in axons (55), suggesting that subcellular structures non-trivially affect the mobility of membrane proteins. Furthermore, the interferometric nature of iSCAT enabled the observation of three-dimensional motion of the molecule on the circumference of the tube-like axon structure (**Figure 3e**). More recently, SPT on living cells was demonstrated with microsecond temporal resolution and nanometer spatial precision in three dimensions (56).

An alternative approach to reducing scattering background from the cell involves performing the measurement in transmission, because it avoids collecting reflections from the powerful combination of nearby glass-water and cell-water interfaces (57, 58). Although the tracked objects in recent reports were comparatively large (>200-nm virus particles and vesicles), there is clear opportunity for future improvements in sensitivity. In addition, more sophisticated background-estimation methods may further extend the applicability of iSCAT-based SPT, as exemplified in recent work that estimates the background in cases where the particle of interest moves by less than the size of the diffraction-limited PSF (59).

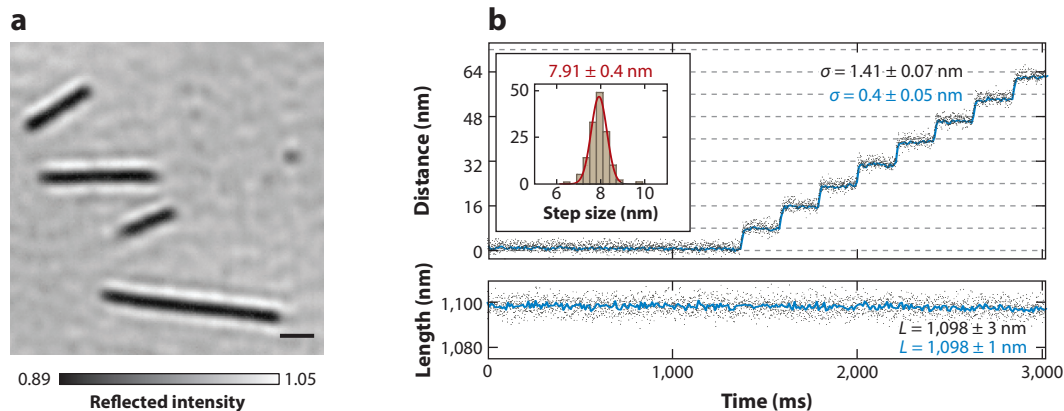


Figure 4

Label-free single-particle tracking. (a) Interferometric scattering microscopy image of individual microtubules bound to microscope cover glass. Scale bar: 0.5 μm . (b) Tracking of artificial 8-nm steps performed by moving the sample of microtubules bound to cover glass with a nanometric stage (*top*) and accompanying measurement of the length of the microtubule as it is translated (*bottom*): Gray dots represent localization acquired at 1 kHz frame rate and the blue line represents localization after averaging to 100 Hz. Figure adapted from Reference 60 with permission from Elsevier.

2.4. Label-Free Single-Particle Tracking

Although the large scattering contrast of GNPs makes them particularly attractive as labels, it is clear from Equation 2 that any object with a refractive index different from that of the surrounding medium will scatter light. This property provides a route to high-SNR visualization of assemblies of biological materials such as proteins and lipids, without the need for labeling. Noting that the contrast of an individual microtubule in iSCAT is rather similar to that of a 20-nm-diameter GNP (27), one would expect similar levels of spatiotemporal precision to be achievable. Indeed, under essentially identical imaging conditions as in Reference 45, the center of mass of individual microtubules (Figure 4a) could be determined with a localization precision of 1.4 nm at 1 kHz, improving to 0.4 nm at 100 Hz (Figure 4b) (60). This is sufficient to distinguish not only the 8-nm steps characteristic of a microtubule bound to a single kinesin motor, but also smaller steps of 4 nm and 2 nm at higher motor densities. In addition to following the center of mass, the length of the microtubules could also be followed with a precision of 1 nm at 100 Hz (Figure 4b), which, in combination with the lack of photobleaching, meant that the shrinkage of microtubules upon washout of taxol could be followed with high spatiotemporal precision over long timescales. Given that most individual proteins are of diameter >2 nm, these results illustrate that in principle it should be possible to monitor the dynamics of biological assemblies at the single-molecule level in a universally applicable way.

3. IMAGING NANOSCOPIC (DIS)ASSEMBLY

The fact that the interferometric contrast relies on a difference in optical properties of the object compared with its surroundings implies that iSCAT can be viewed more generally as a highly sensitive refractive index microscope in the sense that any nanoscopic changes in optical properties can in principle be detected and quantified. To illustrate this, consider the hypothetical (dis)assembly of a nanoscopic structure, such as a GNP, on a glass substrate in solution (Figure 5a). In the absence of the particle, we would expect no spatially distinct scattering signal

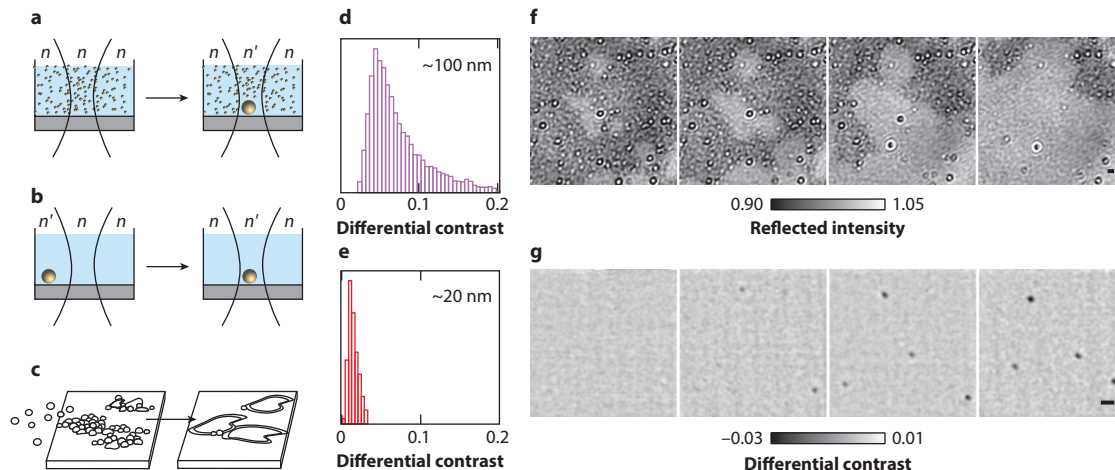


Figure 5

Label-free imaging of nanoscopic (dis)assembly. (a) Schematic of nanoparticle assembly, leading to a local refractive index change that can be visualized in interferometric scattering microscopy (iSCAT). (b) Schematic of nanoparticle motion as a local refractive index modulation. (c) Schematic of the transition from vesicles adsorbing to a glass surface, to a supported lipid bilayer. (d) Histogram of iSCAT contrasts of 100-nm extruded unilamellar vesicles. (e) Histogram of iSCAT contrasts of 20-nm sonicated unilamellar vesicles. (f) Sequence of iSCAT images showing the transition from adsorbed sonicated unilamellar vesicles to a supported lipid bilayer on a glass surface. Images are separated by 200-ms intervals. Scale bar: 1 μm . (g) Sequence of iSCAT images separated by 1 s showing the appearance of lipid nanodomains upon cooling of a three-component droplet interface bilayer below the transition temperature. Scale bar: 1 μm . Panels c–f adapted with permission from Reference 61; copyright 2013 American Chemical Society. Panel g adapted from Reference 65.

from the diffraction-limited volume, because the optical properties of said volume are indistinguishable from the surrounding bulk. This situation changes upon assembly of the GNP, because the local optical properties have now changed, as the local concentration of gold atoms has increased within the diffraction-limited volume.

As a result, iSCAT can be used to monitor not only the motion of objects with high spatiotemporal resolution but also changes to their structure such as their formation or disassembly (see sidebar titled Extinction or Reflectivity?). In fact, even SPT can be regarded as a special form of the more general concept of local changes in optical properties (Figure 5b), just with different underlying dynamics in that the object moves, rather than forming, disappearing, or binding/unbinding.

EXTINCTION OR REFLECTIVITY?

A highly simplified, but potentially very useful way to think about iSCAT imaging is to completely abandon the concepts of extinction and interference and think about changes in surface reflectivity. According to the Fresnel equations, the reflectivity of an interface for normal incidence is given by $R = \left| \frac{n_1 - n_2}{n_1 + n_2} \right|^2$, where n_1 and n_2 are the refractive indices of the two bulk materials forming the interface. In the absence of an object at the interface, $n_1 = n_{\text{glass}}$ and $n_2 = n_{\text{H}_2\text{O}}$, but in its presence $n_2 \neq n_{\text{H}_2\text{O}}$, causing a local change in reflectivity, which can then be detected and imaged. Although these considerations clearly ignore the subtleties at play, they distill the problem to a very simple scenario: iSCAT microscopy, just like interference reflection microscopy or reflection interference contrast microscopy, is a tool that images the reflectivity of an interface. The higher the sensitivity, the smaller the local change in refractive index that can be measured.

3.1. Lipid Assemblies and Their Dynamics

A well-studied but difficult to visualize example of nanoscopic dynamics is the formation of supported lipid bilayers by the vesicle fusion method, which involves the transition of a lipid bilayer from a nanoscopic sphere to a supported sheet (**Figure 5c**). Given that the optical properties of a lipid bilayer are different from those of glass or water, iSCAT can be used to visualize individual vesicles bound to microscope cover glass directly, with a signal that scales with the average particle diameter (**Figure 5d,e**) (61). Importantly, however, rupture of the vesicles on the glass surface to form a planar bilayer causes a change in the amount of material present in a diffraction-limited spot because of the difference in surface area of a sphere compared with that of a disk. As a result, iSCAT can monitor not only the adsorption of single vesicles to a glass substrate, which is the first step in the formation of supported lipid bilayers, but also their rupture, which is the critical next event (**Figure 5f**). Combining these observations with changes to vesicle size and substrate properties enables the direct observation and characterization of supported lipid bilayer formation, revealing the interplay between factors such as critical concentration of surface-bound vesicles and the surface-substrate interaction strength.

The concept of imaging changes in local refractive index can also be applied to dynamics within the membrane, such as local phase separation. Such processes have traditionally been visualized using fluorescence imaging with dye molecules that preferentially compartmentalize in one of the different membrane phases (62–64). Phase separation often involves differences in lipid order and membrane thickness, with associated differences in the local reflectivity that can be imaged with iSCAT. As a result, the appearance and growth of lipid nanodomains upon cooling a bilayer membrane near a phase boundary could be monitored directly with iSCAT in the first dynamic observation of such structures (**Figure 5g**) (65). The dependence of the iSCAT signal on domain size and the ability to quantify simultaneously the mobility of the domains enabled characterization of domain size down to a 50-nm radius. The same concept could also be applied to more complex cholesterol-containing bilayers, which are more closely representative of cellular membranes.

3.2. Virus Particle Dynamics

A virus containing its packaged DNA possesses a different scattering cross section, and therefore different iSCAT contrast, than does an empty viral capsid (**Figure 6a**) (28, 66). As a result, it is possible to quantitatively probe the dynamics of DNA ejection by immobilized bacteriophages upon interaction with the receptor protein LamB (**Figure 6b**) (67). By following the intensity of the iSCAT signal from individual phages as a function of time, the kinetics of material loss can be quantified with higher temporal resolution than possible with previous single-particle studies, an important consideration for a process that occurs on the sub-10-s timescale (68), with a measurement uncertainty equivalent to 4.2 kbp per frame (**Figure 6c**). This corresponds to monitoring the DNA content of individual phages to within 10% of the total content. Aside from DNA release, the same approach is also applicable to the direct monitoring of single virus particle assembly (69). Here, rather than quantifying DNA release, the label-free imaging sensitivity of iSCAT is used to visualize the increase in local protein concentration associated with capsid assembly.

4. LABEL-FREE SINGLE-MOLECULE IMAGING AND QUANTIFICATION

With respect to the possibility of detecting and imaging individual biomolecules, considering microtubules once again proves informative. iSCAT images of individual microtubules bound to a microscope cover glass (**Figure 4a**) provide a signal-to-background ratio on the order of 10,

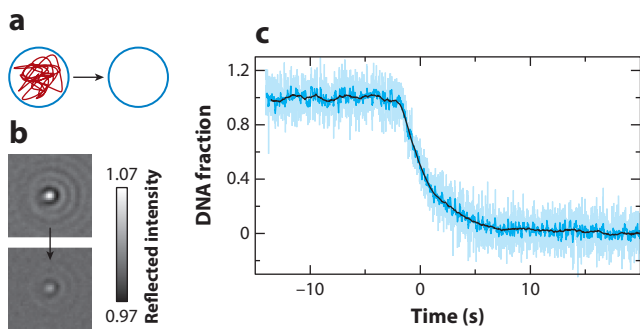


Figure 6

Viral capsid dynamics. (a) Schematic of the difference between a viral capsid with packaged DNA and after DNA ejection. (b) Interferometric scattering microscopy (iSCAT) images of full and empty bacteriophages. (c) Time trace of the DNA content of an immobilized bacteriophage upon addition of LamB, as measured by iSCAT contrast: raw (100 Hz) trace (*light blue*), trace after applying a tenfold moving average (*dark blue*), and trace after a 100-fold moving average (*black*). Panels *b* and *c* adapted with permission from Reference 67; copyright 2016 American Chemical Society.

suggesting a detection limit of approximately 30 tubulin dimers. The fact that the background is constant and can be accurately quantified, however, suggests that the achievable sensitivity of iSCAT is much better than 30 proteins, assuming that the background can be either removed or subtracted, in the spirit of fluorescence detection or the original ion-detection work. This speckle-like background has been persistent in all iSCAT studies and is likely caused by imperfections on and near the surface of microscope cover glass.

It is therefore unsurprising that the first reports of fluorescence-free single-molecule detection at room temperature, which emerged almost simultaneously, used a combination of sophisticated noise and background suppression methodologies to extract the desired single-molecule signal. The experimentally simplest approach removed background signatures by immersing the molecule in an index-matched matrix and eliminating laser-based intensity fluctuations with a balanced detection scheme. The result was sensitivity below parts per million in a transmission equivalent of the work by Lindfors et al. (26), the single-molecule version of an absorption spectrometer, revealing clear signatures of single absorbers (70, 71). Detection of single molecules was also reported with a photothermal approach (72) similar to the original GNP work (25) that capitalized on the excellent background suppression of photothermal microscopy. These studies were complemented simultaneously by a related ground-state depletion approach (73).

These achievements were transformative in that they shattered the notion that room-temperature single-molecule detection was feasible only using fluorescence as a contrast mechanism. All of these approaches, however, relied either on the presence of a strong, resonant electric dipole transition as in single-molecule fluorescence imaging or on quenchers. As a result, they only slightly broadened the scope of single-molecule imaging, because all continued to require that the molecule of interest possesses a resonant response at the illumination wavelength to generate sufficient imaging contrast. Enabling the full promise of label-free single-molecule detection, especially in the biological context of single proteins, required a different approach.

4.1. Nonresonant Single-Protein Detection and Imaging

The other route to visualizing single molecules involves quantifying the background precisely and comparing images with and without the molecule of interest. This approach is no different from

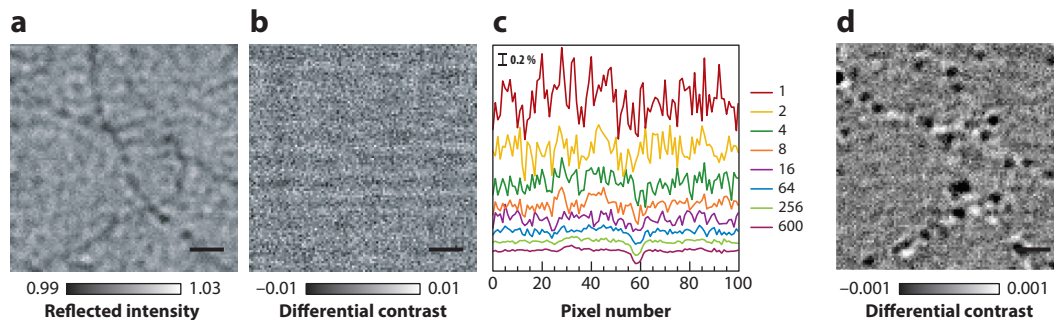


Figure 7

Nonresonant label-free imaging of single biomolecules. (a) Raw interferometric scattering microscopy image of actin filaments on a microscope cover glass in the presence of myosin 5a. (b) Differential image obtained by subtracting the temporal median image of a stack from the raw image in panel a. (c) Line cuts across averaged differential images, illustrating the reduction in shot noise–induced background fluctuations as a function of the number of frames averaged, enabling the observation of a signal from an individual myosin 5a molecule. (d) Differential image of individual myosin 5a molecules obtained by averaging 170 consecutive differential frames. Scale bars: 1 μm . Figure adapted from Reference 74; copyright 2014 American Chemical Society.

the operation of essentially any sensor, which, by definition, compares a readout in the presence and absence of the analyte. For an optimized iSCAT experiment, this requires efficient suppression of noise sources such as sample drift or illumination noise. Under these conditions, it is irrelevant that the single-molecule signal is much smaller than the background because the background can be removed.

To illustrate this approach, consider the first label-free detection, imaging, and tracking of single proteins, illustrated by myosin 5 molecules walking along actin (74). A raw iSCAT image exhibits the now well-known speckle-like background from the microscope cover-glass substrate as well as faint elongated features that can be attributed to single actin filaments (Figure 7a). The assignment to single filaments is robust assuming linear scaling of iSCAT signal with particle volume: Given that individual SV40 virus-like particles of mass 15 MDa produce an iSCAT signal of 4.5%, we would expect single actin filaments, which contain approximately 75 actin subunits (with a total mass of 3.1 MDa) per diffraction-limited spot, to exhibit an iSCAT signal on the order of 0.9%, in excellent agreement with the experimental observation. On the basis of these considerations, we can also calculate the expected signal (0.15%) from individual motor molecules (502-kDa, tail-truncated myosin 5 construct). Taken together, these findings immediately make clear that individual motors cannot be observed statically because their signal is smaller than that of actin filaments, which are visible only with an SNR of ~ 3 .

To visualize single proteins, therefore, the two approaches described above are combined: First, the static background is removed by taking the median image across the stack of images in a movie containing mobile features and subtracting this from all images in the stack (Figure 7b). Second, (background-subtracted) images are averaged to reduce shot noise–induced fluctuations to a level below the signal of individual motors (Figure 7c). Thus, the images reveal mobile, diffraction-limited features colocalized with the filaments and of contrast $0.18 \pm 0.06\%$, as expected for individual motors (Figure 7d). These results, in combination with the expected processivities, step sizes, and velocities, confirm that iSCAT is capable of detecting and imaging individual proteins with a signal magnitude that scales roughly linearly with molecular mass. Demonstrating detection of proteins down to 66 kDa, a related study subsequently used rapid binding to a coverslip surface, rather than motion across objects attached to it, to identify and subtract background features (75).

4.2. Toward Quantitative Label-Free Single-Molecule Microscopy

Despite these successes, the collection of sufficient photons not only to detect single molecules, but also to image them with sufficient precision to enable quantitative studies remained a significant experimental challenge. Detection of the signal from a ~ 500 -kDa myosin 5 molecule with an SNR of 10 requires collection of $\sim 10^8$ photoelectrons, which is orders of magnitude higher than the full well capacity of current digital cameras. As a result, careful combination of spatial and temporal averaging was needed in these initial studies to visualize single molecules.

An appealing alternative would be to attenuate the reference field (r in Equation 1), thereby increasing the interferometric contrast while reducing the amount of light at the detector. This could in principle be achieved by tuning the reflectivity of the glass-water interface by index matching (26), albeit at the expense of biological compatibility. Specific antireflection coatings on the substrate could similarly be used, but they reduce the practicality and simplicity of commercially available cover-glass substrates.

A more practical and tunable approach takes advantage of the ability to distinguish between reflected and scattered light on the basis of their spatial distributions in the back focal plane of the microscope objective. A substantial portion of the emission from a point scatterer near a glass-water interface is concentrated in high numerical apertures of collection, particularly at and above the critical angle. By contrast, the reflected (and illuminating) light, corresponding to wide-field illumination at the sample plane, occupies a small central portion of the back focal plane. As a result, positioning a small, partially reflective mask in or near to the back focal plane of the microscope objective (or a conjugate plane thereof) can attenuate the reflected light by a factor of 100 or more, while only minimally reducing the collection of light scattered by a molecule at the surface (76, 77). Although, as highlighted in the comparison between transmission and reflection in Section 1, this does not in principle improve the shot noise-limited SNR because both the single-molecule contrast and the shot noise-induced fluctuations increase with the square root of the attenuation factor, it is nevertheless advantageous in two regards. First, the reduction of light intensity reaching the detector (by up to 4 orders of magnitude) for a given illumination intensity enables a much better match between the number of photoelectrons that need to be collected for a given SNR and the full well capacity of the detector, thereby reducing the amount of averaging required. Second, it enables the use of cameras that are more efficient at detecting light than are the high full well cameras otherwise necessary.

4.3. Mass Photometry

Although it has thus far been implicit (and intuitive) that smaller proteins give rise to smaller scattering signals, closer inspection of Equation 2 suggests a more quantitative analysis may be fruitful. The interferometric contrast depends on the difference in refractive index between a particle and the surrounding medium, and it increases linearly with volume. Under the assumption that proteins all have similar optical properties and densities, the interferometric contrast should thus be proportional to the protein mass. Indeed, a calculation based on additive contributions of the individual amino acids in a protein sequence to specific volume, refractivity, and mass, when calculated for $>10^5$ protein sequences over six species, gave approximately normal distributions of both refractive index and specific volume, with standard deviations of 0.3% and 1.2% of the mean, respectively (78). This raises the prospect of using interferometric contrast as an absolute measure of molecular mass with a few-percent mass accuracy.

Experimentally, the improvements brought about by numerical aperture filtering in detection, together with an optimized data analysis routine, enabled high SNR imaging and thus highly accurate determination of the interferometric contrast of each molecular binding event (**Figure 8a**). By measuring many such events, a distribution of contrasts could be built up molecule by molecule

Full well capacity:
number of
photoelectrons a single
pixel of a camera can
collect per exposure
before saturation

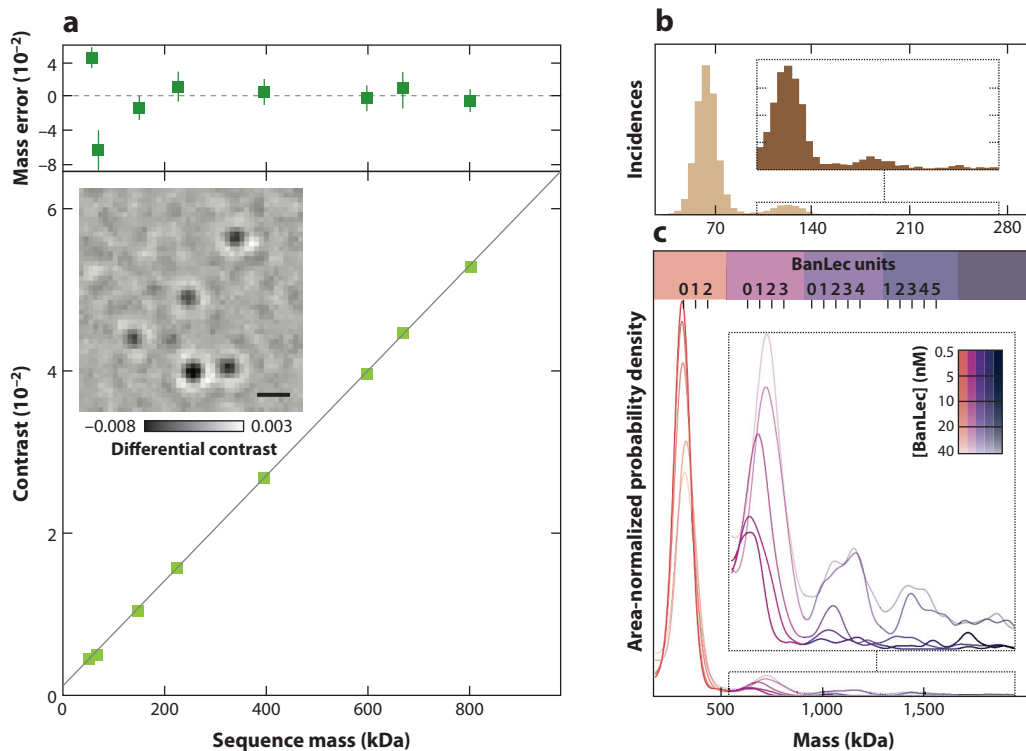


Figure 8

Mass photometry. (a) Single-molecule interferometric scattering microscopy contrast as a function of sequence mass of the protein, including a corresponding linear fit. Deviations from the linear fit are displayed at the top, with error bars denoting the standard error of the mean determined from repeated measurements. (Inset) Differential image of individual BSA molecules binding nonspecifically to a coverslip surface. Scale bar: 0.5 μm . (b) Mass histogram of BSA, with $n = 12,209$ molecules measured. (Inset) Zoom of higher-mass species. (c) Mass distributions of HIV glycoprotein Env as a function of BanLec concentration. Cross-linking induced by BanLec causes an increase in the proportion of higher-order species rather than binding, which would cause a mass shift. (Inset) Zoom of the higher-mass species. Figure adapted from Reference 78 with permission from AAAS.

and the average contrast for a given molecular weight species determined. A plot of mean contrast against sequence mass for a range of proteins verified the expected linear relationship, with an average error (defined as the deviation of a data point from a linear fit) of 2% of the sequence mass (**Figure 8a**) (78). The width of the distribution arising from a single molecular species, which arises from the precision with which the contrast of each molecule can be measured, defines the resolution of the microscope's performance as a mass measurement device and reaches values as low as 19 kDa (full width at half maximum). This parameter is of the utmost importance because it enables clear separation of different oligomeric states (**Figure 8b**), which is critical for both structural and interaction studies. The precision with which the center of the distribution could be determined in repeated experiments was $\sim 2\%$ of the molecular mass, approaching the levels required to detect small-molecule binding.

The concept of using such a microscope as a biomolecular mass measurement device may prove a useful analytical tool, especially for the characterization of samples exhibiting heterogeneity, multistep assembly mechanisms, or protein-ligand interactions. Compared with other solution-based techniques, this approach exhibits high mass resolution, whereas the single-molecule basis of the technique addresses often-encountered issues associated with sample heterogeneity through

the ability to count even very rare species in the presence of many other molecules of different mass, such as the 0.25% abundant BSA tetramer (**Figure 8b**). Although mass photometry cannot hope to match the resolution and accuracy of native mass spectrometry in the gas phase, its ease of use and compatibility with essentially any buffer conditions make it a highly valuable and competitive addition to the bioanalytical toolbox.

Several aspects of the achievable capabilities are well illustrated by a comparatively simple experiment on a rather complicated system: the interaction of the HIV inhibitor BanLec (60 kDa) with the HIV envelope protein (~300 kDa) (79–81). Recording the mass distributions of the system as a function of BanLec concentration reveals a reduction in monomer species, with a concomitant increase in dimers and higher-order oligomers (**Figure 8c**). This behavior directly points toward a cross-linking, rather than a coating, mechanism, which would have simply resulted in a mass shift of the monomer species to higher molecular weight. This intuitive analysis can be quantified by segmenting the mass spectra into different oligomeric species and determining their mole fractions as a function of BanLec concentration, yielding quantitative information on the aggregation mechanism and the associated energetics.

4.4. Mass Imaging

A key advantage of employing an imaging-based approach is that one can not only detect and determine the molecular mass of single biomolecules but also perform these measurements with high temporal resolution and spatial precision. To illustrate this, consider the well-known phenomenon of actin polymerization. Combining label-free imaging precision with single-molecule mass sensitivity enabled direct observation of the growth (**Figure 9a**) and stepwise changes in the length of surface-immobilized actin filaments under polymerizing conditions (**Figure 9b**).

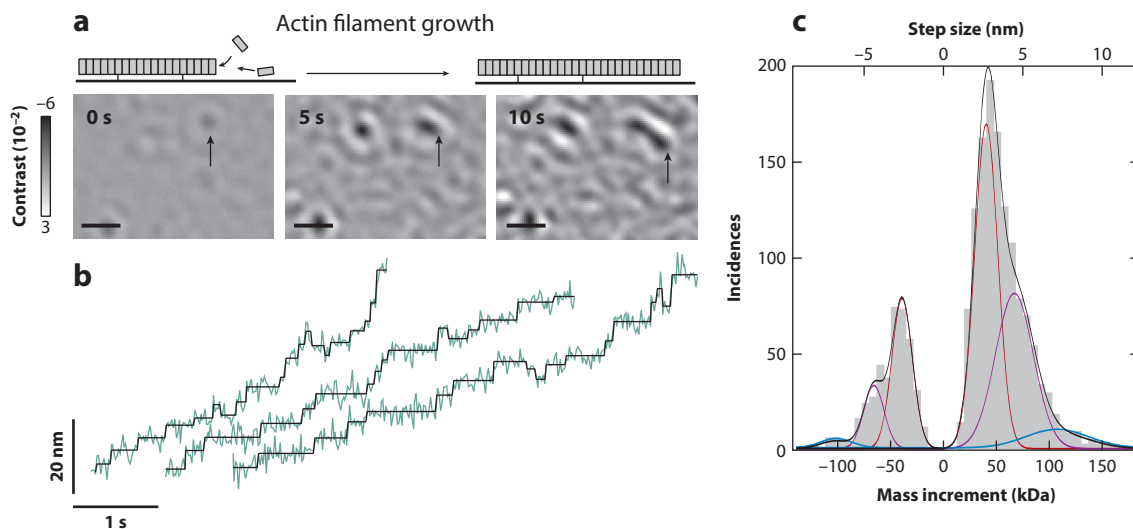


Figure 9

Label-free mass imaging of actin polymerization at the single-molecule level. (a) Schematic and interferometric scattering microscopy image sequence of actin filaments polymerizing near a cover-glass surface. Scale bars: 1 μm . (b) Traces of actin filament tip position over time (green), with corresponding detected steps (black). (c) Step size and mass histogram from 1,523 steps and 33 filaments, including a fit to a Gaussian mixture model (black) and individual contributions: monomer (orange), dimer (purple), and trimer (blue). Figure adapted from Reference 78 with permission from AAAS.

Analysis of these traces revealed length changes at multiples of 2.7 nm and associated mass changes of ~40 kDa, in good agreement with expectations based on the size and mass of monomeric actin (Figure 9c). Moreover, the resulting on/off rates as well as their relative magnitude match those expected from ensemble studies of actin polymerization (82–85), confirming the direct observation of single-molecule dynamics.

5. CONCLUSION

Ultrasensitive optical microscopy has undergone dramatic changes over the past three decades, with broad implications for imaging biological structure and dynamics as well as for bioanalytics. The dominance of fluorescence-based approaches, in particular for *in vitro* studies, has recently been challenged by extinction-based methodologies. As always, such a drastic change of contrast mechanism is accompanied by both advantages and disadvantages, which have to be considered carefully when deciding which approach to use to address the question of interest. Nevertheless, there is now clear evidence that iSCAT can provide uniquely detailed information in three areas: (a) SPT with up to microsecond temporal resolution and subnanometer spatial precision when labels of 20-nm diameter or larger are acceptable; (b) label-free imaging of nanoscale (dis)assembly with high spatiotemporal precision; and (c) direct optical detection, imaging, and mass measurement of single biomolecules in solution. These capabilities do not focus on one specific problem, but instead cover a tremendous breadth of biological systems and questions, demonstrating the potential of iSCAT for studying nanoscale phenomena down to the single-molecule level. What is most exciting, however, is the realization that this technology is very much still in its infancy, in particular, in the context of single-molecule bioanalytical applications such as mass photometry. If only a fraction of the creativity, effort, and innovation that has been directed at single-molecule fluorescence-based techniques over the past decades can be applied to interference-based microscopy, it will likely become a transformative method for providing quantitative information on the structure and dynamics of a wide range of nanoscale processes.

SUMMARY POINTS

1. Both extinction- and interference-based microscopy significantly expand the potential applications of ultrasensitive microscopy beyond simply avoiding the need for fluorescent labeling.
2. High-speed and ultraprecise single-particle tracking is instrumental for revealing mechanistic details of nanoscale motion at short timescales and small length scales.
3. Imaging nanoscopic refractive index differences and changes with high sensitivity enables the observation of (dis)assembly processes in a variety of environments and a broad range of species.
4. Careful optimization of the experimental approach enables robust, nonresonant optical detection and imaging of single biomolecules without the need for any labels or other structures for signal enhancement.
5. The close relationship between molecular mass and polarizability of biological macromolecules paves the way to accurate, precise, and highly resolved mass measurement at the single-molecule level.

DISCLOSURE STATEMENT

The authors are academic founders and consultants to Refeyn.

ACKNOWLEDGMENTS

We gratefully acknowledge support for this work from a Zvi and Ofra Meitar Magdalen Graduate Scholarship (G.Y.) and an ERC Starting Investigator Grant (nanoscope, 337757). We thank Anne Straube for the fluorescence and dark-field images in **Figure 1**.

LITERATURE CITED

1. Hooke R. 1665. *Micrographia, or, Some Physiological Descriptions of Minute Bodies Made by Magnifying Glasses: With Observations and Inquiries Thereupon*. London: J Martyn, J Allestry
2. Jiang Y, Chen Z, Han Y, Deb P, Gao H, et al. 2018. Electron ptychography of 2D materials to deep sub-angstrom resolution. *Nature* 559:343–49
3. Neuhauser W, Hohenstatt M, Toschek P, Dehmelt H. 1980. Localized visible Ba⁺ mono-ion oscillator. *Phys. Rev. A* 22:1137
4. **Moerner WE, Kador L. 1989. Optical detection and spectroscopy of single molecules in a solid. *Phys. Rev. Lett.* 62:2535–38**
5. Orrit M, Bernard J. 1990. Single pentacene molecules detected by fluorescence excitation in a p-terphenyl crystal. *Phys. Rev. Lett.* 65:2716–19
6. Siedentopf H, Zsigmondy R. 1902. Über Sichtbarmachung und Größenbestimmung ultramikroskopischer Teilchen, mit besonderer Anwendung auf Golddrubingläser. *Ann. Phys.* 315:1–39
7. Straube A. 2011. How to measure microtubule dynamics? *Methods Mol. Biol.* 777:1–14
8. Streed EW, Jechow A, Norton BG, Kielpinski D. 2012. Absorption imaging of a single atom. *Nat. Commun.* 3:933
9. Bohren CF, Huffman DR. 1983. *Absorption and Scattering of Light by Small Particles*. New York: Wiley
10. Zernike F. 1935. Das Phasenkontrastverfahren bei der mikroskopischen Beobachtung. *Z. Tech. Phys.* 16:454
11. Nomarski G. 1955. Microinterféromètre différentiel à ondes polarisées. *J. Phys. Radium* 16:9
12. Allen R, David G. 1969. The Zeiss-Nomarski differential interference equipment for transmitted-light microscopy. *Z. Wiss. Mikrosk. Mikrosk. Tech.* 69:193–221
13. Kandel ME, Teng KW, Selvin PR, Popescu G. 2017. Label-free imaging of single microtubule dynamics using spatial light interference microscopy. *ACS Nano* 11:647–55
14. Cotte Y, Toy F, Jourdain P, Pavillon N, Boss D, et al. 2013. Marker-free phase nanoscopy. *Nat. Photonics* 7:113–17
15. Kim T, Zhou RJ, Mir M, Babacan SD, Carney PS, et al. 2014. White-light diffraction tomography of unlabelled live cells. *Nat. Photonics* 8:256–63
16. Ortega-Arroyo J, Kukura P. 2012. Interferometric scattering microscopy (iSCAT): new frontiers in ultrafast and ultrasensitive optical microscopy. *Phys. Chem. Chem. Phys.* 14:15625–36
17. **Curtis AS. 1964. The mechanism of adhesion of cells to glass: a study by interference reflection microscopy. *J. Cell Biol.* 20:199–215**
18. Ploem J. 1975. *Reflection-Contrast Microscopy as a Tool for Investigation of the Attachment of Living Cells to a Glass Surface*. Oxford: Blackwell
19. Gingell D, Todd I. 1979. Interference reflection microscopy. A quantitative theory for image interpretation and its application to cell-substratum separation measurement. *Biophys. J.* 26:507–26
20. Limozin L, Sengupta K. 2009. Quantitative reflection interference contrast microscopy (RICM) in soft matter and cell adhesion. *ChemPhysChem* 10:2752–68
21. Rädler J, Sackmann E. 1993. Imaging optical thicknesses and separation distances of phospholipid vesicles at solid surfaces. *J. Phys. II* 3:727–48

4. Demonstrates the first optical detection of single molecules in a condensed phase.

17. This early work describes interference reflection microscopy and its first application in a biological context.

23. Describes the use of a confocal microscope in reflection mode to image microtubules, filaments of only 25-nm diameter.

26. Demonstrates detection and spectroscopy of gold nanoparticles down to 5-nm diameter in a confocal reflection arrangement.

29. Introduces the term iSCAT and concepts enabling shot noise-limited detection sensitivity below the limit imposed by background scattering.

45. Provides an example of highly precise single-particle tracking of gold-labeled motor proteins at speeds up to 1 kHz.

22. Rädler J, Strey H, Sackmann E. 1995. Phenomenology and kinetics of lipid bilayer spreading on hydrophilic surfaces. *Langmuir* 11:4539–48
23. Amos LA, Amos WB. 1991. The bending of sliding microtubules imaged by confocal light microscopy and negative stain electron microscopy. *J. Cell Sci.* 1991(Suppl. 14):95–101
24. Tsien RY. 1998. The green fluorescent protein. *Annu. Rev. Biochem.* 67:509–44
25. Boyer D, Tamarat P, Maali A, Lounis B, Orrit M. 2002. Photothermal imaging of nanometer-sized metal particles among scatterers. *Science* 297:1160–63
26. Lindfors K, Kalkbrenner T, Stoller P, Sandoghdar V. 2004. Detection and spectroscopy of gold nanoparticles using supercontinuum white light confocal microscopy. *Phys. Rev. Lett.* 93:037401
27. Jacobsen V, Stoller P, Brunner C, Vogel V, Sandoghdar V. 2006. Interferometric optical detection and tracking of very small gold nanoparticles at a water-glass interface. *Opt. Express* 14:405–14
28. Ewers H, Jacobsen V, Klotzsch E, Smith AE, Helenius A, Sandoghdar V. 2007. Label-free optical detection and tracking of single virions bound to their receptors in supported membrane bilayers. *Nano Lett.* 7:2263–66
29. Kukura P, Ewers H, Muller C, Renn A, Helenius A, Sandoghdar V. 2009. High-speed nanoscopic tracking of the position and orientation of a single virus. *Nat. Methods* 6:923–27
30. Shen H, Tauzin LJ, Baiyasi R, Wang W, Moringo N, et al. 2017. Single particle tracking: from theory to biophysical applications. *Chem. Rev.* 117:7331–76
31. Thompson RE, Larson DR, Webb WW. 2002. Precise nanometer localization analysis for individual fluorescent probes. *Biophys. J.* 82:2775–83
32. Yildiz A, Forkey JN, McKinney SA, Ha T, Goldman YE, Selvin PR. 2003. Myosin V walks hand-over-hand: single fluorophore imaging with 1.5-nm localization. *Science* 300:2061–65
33. English BP, Haurlyuk V, Sanamrad A, Tankov S, Dekker NH, Elf J. 2011. Single-molecule investigations of the stringent response machinery in living bacterial cells. *PNAS* 108:E365–73
34. Uphoff S, Reyes-Lamothe R, Garza de Leon F, Sherratt DJ, Kapanidis AN. 2013. Single-molecule DNA repair in live bacteria. *PNAS* 110:8063–68
35. Balzarotti F, Eilers Y, Gwosch KC, Gynna AH, Westphal V, et al. 2017. Nanometer resolution imaging and tracking of fluorescent molecules with minimal photon fluxes. *Science* 355:606–12
36. Kues T, Peters R, Kubitschek U. 2001. Visualization and tracking of single protein molecules in the cell nucleus. *Biophys. J.* 80:2954–67
37. Kubitschek U, Kuckmann O, Kues T, Peters R. 2000. Imaging and tracking of single GFP molecules in solution. *Biophys. J.* 78:2170–79
38. Seisenberger G, Ried MU, Endress T, Buning H, Hallek M, Brauchle C. 2001. Real-time single-molecule imaging of the infection pathway of an adeno-associated virus. *Science* 294:1929–32
39. Yildiz A, Selvin PR. 2005. Fluorescence imaging with one nanometer accuracy: application to molecular motors. *Acc. Chem. Res.* 38:574–82
40. Pierobon P, Achouri S, Courty S, Dunn AR, Spudich JA, et al. 2009. Velocity, processivity, and individual steps of single myosin V molecules in live cells. *Biophys. J.* 96:4268–75
41. Trybus KM. 2008. Myosin V from head to tail. *Cell. Mol. Life Sci.* 65:1378–89
42. Warshaw DM, Kennedy GG, Work SS, Kremetsova EB, Beck S, Trybus KM. 2005. Differential labeling of myosin V heads with quantum dots allows direct visualization of hand-over-hand processivity. *Biophys. J.* 88:L30–32
43. Sakamoto T, Webb MR, Forgacs E, White HD, Sellers JR. 2008. Direct observation of the mechanochemical coupling in myosin Va during processive movement. *Nature* 455:128–32
44. Dunn AR, Spudich JA. 2007. Dynamics of the unbound head during myosin V processive translocation. *Nat. Struct. Mol. Biol.* 14:246–48
45. Andrecka J, Ortega Arroyo J, Takagi Y, de Wit G, Fineberg A, et al. 2015. Structural dynamics of myosin 5 during processive motion revealed by interferometric scattering microscopy. *eLife* 4:e05413
46. Mickolajczyk KJ, Deffenbaugh NC, Arroyo JO, Andrecka J, Kukura P, Hancock WO. 2015. Kinetics of nucleotide-dependent structural transitions in the kinesin-1 hydrolysis cycle. *PNAS* 112:E7186–93

47. Andrecka J, Takagi Y, Mickolajczyk KJ, Lippert LG, Sellers JR, et al. 2016. Interferometric scattering microscopy for the study of molecular motors. *Methods Enzymol.* 581:517–39
48. Fujiwara T, Ritchie K, Murakoshi H, Jacobson K, Kusumi A. 2002. Phospholipids undergo hop diffusion in compartmentalized cell membrane. *J. Cell Biol.* 157:1071–81
49. Lin YH, Chang WL, Hsieh CL. 2014. Shot-noise limited localization of single 20 nm gold particles with nanometer spatial precision within microseconds. *Opt. Express* 22:9159–70
50. Spillane KM, Ortega-Arroyo J, de Wit G, Eggeling C, Ewers H, et al. 2014. High-speed single-particle tracking of GM1 in model membranes reveals anomalous diffusion due to interleaflet coupling and molecular pinning. *Nano Lett.* 14:5390–97
51. Spindler S, Ehrig J, König K, Nowak T, Piliarik M, et al. 2016. Visualization of lipids and proteins at high spatial and temporal resolution via interferometric scattering (iSCAT) microscopy. *J. Phys. D* 49:349601
52. Wu HM, Lin YH, Yen TC, Hsieh CL. 2016. Nanoscopic substructures of raft-mimetic liquid-ordered membrane domains revealed by high-speed single-particle tracking. *Sci. Rep.* 6:20542
53. Isojima H, Iino R, Niitani Y, Noji H, Tomishige M. 2016. Direct observation of intermediate states during the stepping motion of kinesin-1. *Nat. Chem. Biol.* 12:290–97
54. de Wit G, Albrecht D, Ewers H, Kukura P. 2018. Revealing compartmentalized diffusion in living cells with interferometric scattering microscopy. *Biophys. J.* 114:2945–50
55. Xu K, Zhong G, Zhuang X. 2013. Actin, spectrin, and associated proteins form a periodic cytoskeletal structure in axons. *Science* 339:452–56
56. Taylor RW, Mahmoodabadi RG, Rauschenberger V, Giessl A, Schambony A, Sandoghdar V. 2018. Interferometric scattering microscopy reveals microsecond nanoscopic protein motion on a live cell membrane. bioRxiv 401133. <https://doi.org/10.1101/401133>
57. Huang YF, Zhuo GY, Chou CY, Lin CH, Chang W, Hsieh CL. 2017. Coherent brightfield microscopy provides the spatiotemporal resolution to study early stage viral infection in live cells. *ACS Nano* 11:2575–85
58. Huang YF, Zhuo GY, Chou CY, Lin CH, Hsieh CL. 2017. Label-free, ultrahigh-speed, 3D observation of bidirectional and correlated intracellular cargo transport by coherent brightfield microscopy. *Nanoscale* 9:6567–74
59. Cheng C-Y, Hsieh C-L. 2017. Background estimation and correction for high-precision localization microscopy. *ACS Photonics* 4:1730–39
60. Andrecka J, Ortega-Arroyo J, Cross R, Kukura P. 2016. Label-free imaging of microtubules with sub-nanometer precision using interferometric scattering microscopy. *Biophys. J.* 110(1):214–17
61. Andrecka J, Spillane KM, Ortega-Arroyo J, Kukura P. 2013. Direct observation and control of supported lipid bilayer formation with interferometric scattering microscopy. *ACS Nano* 7:10662–70
62. Veatch SL, Keller SL. 2005. Seeing spots: complex phase behavior in simple membranes. *Biochim. Biophys. Acta* 1746:172–85
63. Dietrich C, Bagatolli LA, Volovyk ZN, Thompson NL, Levi M, et al. 2001. Lipid rafts reconstituted in model membranes. *Biophys. J.* 80:1417–28
64. Baumgart T, Hammond AT, Sengupta P, Hess ST, Holowka DA, et al. 2007. Large-scale fluid/fluid phase separation of proteins and lipids in giant plasma membrane vesicles. *PNAS* 104:3165–70
65. de Wit G, Danial JS, Kukura P, Wallace MI. 2015. Dynamic label-free imaging of lipid nanodomains. *PNAS* 112:12299–303
66. de Frutos M, Letellier L, Raspaud E. 2005. DNA ejection from bacteriophage T5: analysis of the kinetics and energetics. *Biophys. J.* 88:1364–70
67. Goldfain AM, Garmann RF, Jin Y, Lahini Y, Manoharan VN. 2016. Dynamic measurements of the position, orientation, and DNA content of individual unlabeled bacteriophages. *J. Phys. Chem. B* 120:6130–38
68. Grayson P, Han L, Winther T, Phillips R. 2007. Real-time observations of single bacteriophage λ DNA ejections in vitro. *PNAS* 104:14652–57
69. Garmann RF, Goldfain AM, Manoharan VN. 2018. Measuring the self-assembly kinetics of individual viral capsids. bioRxiv 265330. <https://doi.org/10.1101/265330>
70. Celebrano M, Kukura P, Renn A, Sandoghdar V. 2011. Single-molecule imaging by optical absorption. *Nat. Photonics* 5:95
49. Demonstrates high-speed tracking of 20-nm gold nanoparticles at 500 kHz with a localization precision of 2 nm.

74. Demonstrates the first all-optical nonresonant detection of individual, unlabeled proteins.

76. Explains the concept and implementation of numerical aperture filtering for enhanced interferometric contrast.

78. Demonstrates the concept of using interferometric contrast of single biomolecules for quantitative measurements of their mass.

71. Kukura P, Celebrano M, Renn A, Sandoghdar V. 2010. Single-molecule sensitivity in optical absorption at room temperature. *J. Phys. Chem. Lett.* 1:3323–27
72. Gaiduk A, Yorulmaz M, Ruijgrok PV, Orrit M. 2010. Room-temperature detection of a single molecule's absorption by photothermal contrast. *Science* 330:353–56
73. Chong S, Min W, Xie XS. 2010. Ground-state depletion microscopy: detection sensitivity of single-molecule optical absorption at room temperature. *J. Phys. Chem. Lett.* 1:3316–22
74. **Ortega Arroyo J, Andrecka J, Spillane KM, Billington N, Takagi Y, et al. 2014. Label-free, all-optical detection, imaging, and tracking of a single protein. *Nano Lett.* 14:2065–70**
75. Piliarik M, Sandoghdar V. 2014. Direct optical sensing of single unlabelled proteins and super-resolution imaging of their binding sites. *Nat. Commun.* 5:4495
76. **Cole D, Young G, Weigel A, Sebesta A, Kukura P. 2017. Label-free single-molecule imaging with numerical-aperture-shaped interferometric scattering microscopy. *ACS Photonics* 4:211–16**
77. Liebel M, Hugall JT, van Hulst NF. 2017. Ultrasensitive label-free nanosensing and high-speed tracking of single proteins. *Nano Lett.* 17:1277–81
78. **Young G, Hundt N, Cole D, Fineberg A, Andrecka J, et al. 2018. Quantitative mass imaging of single biological macromolecules. *Science* 360:423–27**
79. Swanson MD, Winter HC, Goldstein IJ, Markovitz DM. 2010. A lectin isolated from bananas is a potent inhibitor of HIV replication. *J. Biol. Chem.* 285:8646–55
80. Hopper JTS, Ambrose S, Grant OC, Krumm SA, Allison TM, et al. 2017. The tetrameric plant lectin BanLec neutralizes HIV through bidentate binding to specific viral glycans. *Structure* 25:773–82.e5
81. Lusvarghi S, Lohith K, Morin-Leisk J, Ghirlando R, Hinshaw JE, Bewley CA. 2016. Binding site geometry and subdomain valency control effects of neutralizing lectins on HIV-1 viral particles. *ACS Infect. Dis.* 2:882–91
82. Tobacman LS, Korn ED. 1983. The kinetics of actin nucleation and polymerization. *J. Biol. Chem.* 258:3207–14
83. Carlier MF, Pantaloni D. 1986. Direct evidence for ADP-Pi-F-actin as the major intermediate in ATP-actin polymerization. Rate of dissociation of Pi from actin filaments. *Biochemistry* 25:7789–92
84. Wegner A, Engel J. 1975. Kinetics of the cooperative association of actin to actin filaments. *Biophys. Chem.* 3:215–25
85. Pollard TD. 1986. Rate constants for the reactions of ATP- and ADP-actin with the ends of actin filaments. *J. Cell Biol.* 103:2747–54